Cyclic hardening/softening and deformation mechanisms of a twip steel under reversed loading

C. d'Hondt, V. Doquet, J.P. Couzinié

To cite this version:

C. d'Hondt, V. Doquet, J.P. Couzinié. Cyclic hardening/softening and deformation mechanisms of a twip steel under reversed loading. Materialia, 2022, 22, pp.101421. 10.1016/j.mtla.2022.101421 . hal-03699897

Materialia 22 (2022) 101421 https://doi.org/10.1016/j.mtla.2022.101421

CYCLIC HARDENING/SOFTENING AND DEFORMATION MECHANISMS OF A TWIP STEEL UNDER REVERSED LOADING

C. D'Hondt[1,2], V. Doquet[1]*, J.P. Couzinié[2]

[1]CNRS UMR 7649, Laboratoire de Mécanique des Solides,

Ecole Polytechnique - Institut Polytechnique de Paris, 91128 Palaiseau, France

[2] Univ Paris Est Creteil, CNRS, ICMPE, UMR 7182, 2 rue Henri Dunant, 94320 Thiais, France

**Corresponding author: doquet@lms.polytechnique.fr*

Abstract: Push-pull tests at fixed plastic strain amplitude or fixed stress amplitude were run on a TWIP steel, and followed by TEM observations, to analyze its cyclic behavior in relation with the deformation mechanisms. The kinematic and isotropic components of the flow stress were measured throughout the whole cyclic hardening/softening stages, and their evolution with the cumulated plastic strain was compared to those measured in tension. The rise of the internal stress was found responsible for the initial cyclic hardening, but this stress reached at most 50 % of the flow stress, as compared to nearly 70% in tension. Special constitutive equations were identified to capture these evolutions, as well as the transition from hardening to softening. Both components of the flow stress slightly decrease during the softening stage, whose origin is discussed, based on TEM observations at peak stress amplitude, or after softening. The present measurements and TEM observations, combined with those from a previous study of twinning/detwinning kinetics in push-pull on the same steel [29], suggest that under cyclic loading, mechanical twinning cannot be responsible for significant kinematic hardening of intragranular nature (or "dynamic Hall-Petch effect"), but rather contributes to a back stress of intergranular origin.

Keywords: TWIP steel; cyclic plasticity; kinematic hardening; twinning; Short Range Order; constitutive equations

1. Introduction

After a long period during which research on TWIP steels focused almost exclusively on their tensile behavior [1,2], their cyclic behavior started to attract more attention during the last decade [3–23]. This was aroused by potential applications, in which the steel would undergo cyclic loading. To design fatigue-resistant structures, the stresses and strains in stress concentration areas have to be determined, through elastic-plastic finite elements (FE) computations, and then used as an input in fatigue criteria. However, constitutive equations capturing the complex cyclic behavior of TWIP steels in a form suitable for structural FE simulations do not seem to be available in the literature. Even though the cyclic hardening and softening stages can be relatively short, compared to the entire fatigue lives, it is nonetheless important to understand their origin, and to model it properly, since they determine the steady-state plastic strain and stress amplitudes that control fatigue lives.

Most studies on the cyclic behavior of Fe-Mn-C steels were based on fully reversed, strain-controlled tension-compression tests, followed by TEM or ECCI observations. In most studies, a fast cyclic hardening stage was observed, followed by a saturation stage, at low or intermediate amplitudes, and by continuous cyclic softening until fracture, at high amplitudes. The degree of initial cyclic hardening was shown to increase with the strain rate [20]. This was explained by a more pronounced increase of the dislocation density when dynamic strain aging (DSA) appears, due to interactions between gliding dislocations and C-Mn Short Range Order (SRO) zones. The initial cyclic hardening was also shown to increase sharply with the C content, and thus with the density of C-Mn complexes. The increase in carbon content is indeed responsible for a transition from wavy to planar slip, despite the increase in the Stacking Fault Energy (SFE) [4,8]. The more pronounced initial cyclic hardening at large C content was associated with more profuse twinning at large strain amplitude, and with a higher cyclic hardening exponent, and more fusiform stress-strain loops. An increase in Mn content, also leading to an increase in SFE, but with a limited impact on SRO, was found to promote the initial cyclic hardening, but to a much smaller extent than an increase in C content [5]. The increase in Mn content led to a reduction of the twin ability as demonstrated by ECCI observations of thinner, more widely spaced twins. In that respect, the role played by twinning in the cyclic hardening of TWIP steels is not completely clear, and deserves further investigation, since more profuse twinning was sometimes associated with an increased cyclic hardening [4,8] and also with the opposite trend [5].

The duration of the hardening stage was reported in terms of number of cycles (a few tens to a few hundred cycles, depending on the composition, and strain amplitude), or as a fraction of the fatigue life (5 to 20 %) [3,11]. In the present study, it will rather be analyzed in terms of cumulated plastic strain (a parameter that reflects the total amount of irreversible deformation, regardless of the loading path, whether monotonous or alternating), since it allows a comparison between the cyclic and tensile behavior. This might shed light on the underlying mechanisms, and especially on the role of twinning. Chalant & Remy [24] used such an approach to compare the evolutions of the twin fraction in tension and in tension-compression, in a FCC alloy.

The cyclic softening, much more modest than the initial hardening, was reported to increase with the strain amplitude, except at high C content, which promotes a stable post-hardening state [4]. It was attributed to a disordering of C-Mn SRO, and as a consequence, the development of strain localization bands [5], or to a progressive reduction in dislocation density [16,17].

Note that comparisons between different TWIP steels based on push-pull tests run at fixed total strain amplitude could be biased by differences in yield stress associated with different compositions or grain sizes, and thus differences in plastic strain amplitude and plastic strain rate. The later matters, because of DSA. In the present study, most tension-compression tests were run at fixed plastic strain amplitude. Two tests were also run at fixed stress amplitude, for comparison. Cyclic plasticity of TWIP steels under such loading mode has been documented so far only in a few papers [19,23] that rather focused on fatigue damage and reported TEM observations at various stages, but neither stress-strain loops, nor strain amplitude evolutions.

During cyclic hardening under strain control, the stress-strain loops were reported to become more and more elongated [3,10]. This effect, was more pronounced in Fe22Mn0.6C (SFE $\approx$ 21 mJ/m^2) which exhibits more planar slip and profuse twinning in tension-compression, than in Fe-22Mn-0.6C-3Al (SFE $\approx$ 37 mJ/m^2), less prone to twinning [10]. This change in shape of the loops was captured by constitutive equations including a special form of non-linear kinematic hardening [10]. A few measurements of the isotropic and kinematic components of the flow stress of TWIP steels in tension-compression were reported, but only for the first few cycles [10,25], or just at saturation [6]. An attempt to formulate and identify constitutive equations for TWIP steels, usable for finite element design of structures, or numerical analysis of cyclic plasticity at a fatigue crack tip and plasticity-induced closure was made by Yang et al. [10]. It was however limited to the initial hardening stage, and did not capture the transition towards softening. The present work, which includes measurements of the isotropic and kinematic components of the flow stress over the whole hardening/softening sequence, at various plastic strain amplitudes or stress amplitudes proposes an improved model.

After an introduction of the investigated TWIP steel and of the experimental procedures, the tensile and cyclic behaviors, as well as the insight on the deformation mechanisms provided by TEM observations are presented. This leads to a discussion of the relation between those two aspects, and more specifically on the role of mechanical twinning in cyclic hardening, and of the C-Mn SRO in cyclic softening.

2. Experimental procedures

2.1. Material

The study was run on a TWIP steel produced by ArcelorMittal as a 36 mm-thick hot-rolled plate, with the composition given in table 1. For such a composition, a SFE between 21 and 37 mJ.m^{-2} has been reported in the literature [21–23,26]. The microstructure of as-received material was characterized on three orthogonal sections (normal to the rolling direction, RD, normal direction, ND, and transverse direction TD of the plate), using a FEI Quanta 600 XL40-W scanning electron microscope equipped with a Nordlys 2 EBSD detector, the Aztec software for data collection, and the Channel 5 software for data post-treatment. Mappings of grain orientations and grain size histograms were obtained, with a 10° misorientation criterion to detect grain boundaries. The analyzed areas contained approximately 100 grains. No significant difference was found between the three observation planes. The material exhibits equiaxed grains and is nearly texture free (Figure 1). Considering annealing twin boundaries as grain boundaries, the grain size is 23.9 ± 15.7 μm in RD plane, 24.3 ± 17.9 μm in TD plane, and 23.9 ± 16.6 μm in ND plane. If the annealing twins are not considered as grain boundaries, the grain size is 37.9 ± 20.4 μm in RD plane, 37.3 ± 23.4 μm in TD plane, and 40.1 ± 21.9 μm in ND plane.

Table 1

Chemical composition of the TWIP steel (weight %)

Mn	C	V	Si	Cr	P	N	Fe
22.29	0.63	0.20	0.23	0.19	0.03	0.01	bal.

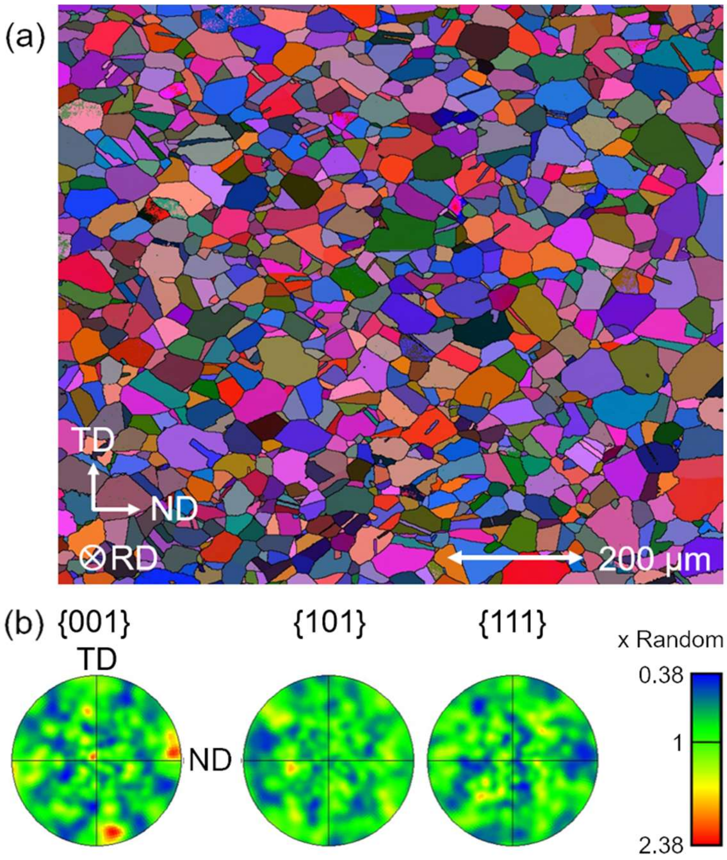

Figure 1: SEM-EBSD analysis of the microstructure of as-received TWIP steel (a) Euler angles map showing equiaxed grains and (b) pole figures showing nearly random texture.

2.2. Test procedures

Cylindrical specimens, 8 mm in diameter and 16 mm in gage length were cut along the RD direction (Fig. 2a), and used for both tensile and fully reversed push-pull tests, run on a MTS 810 testing machine equipped with a ± 100 kN load cell controlled by the TestSuite software. An extensometer with a strain range of ± 15% was used (Fig. 2b). Since the aim of the push-pull tests was not to investigate fatigue damage, but only the cyclic behavior, no surface preparation was done.

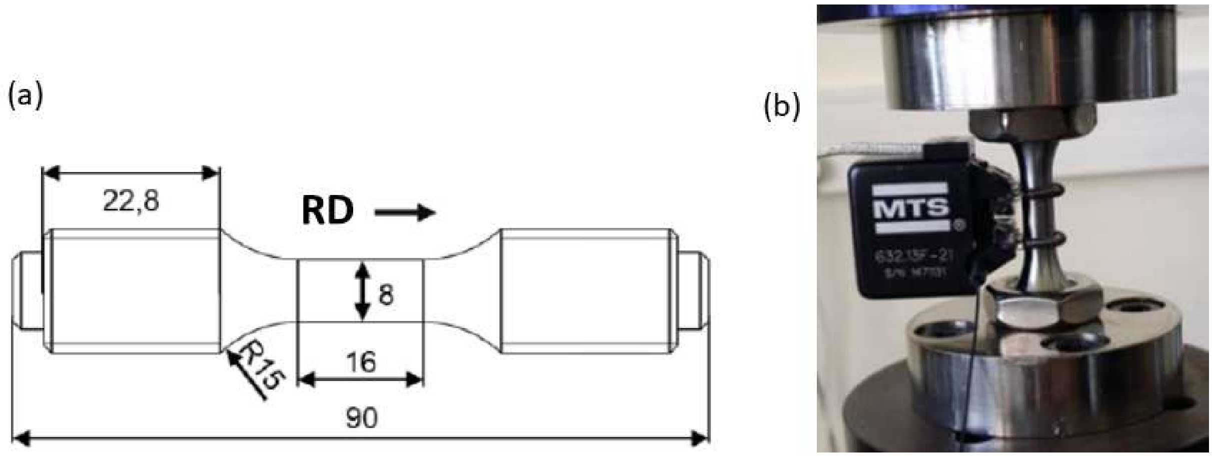

Figure 2: a) Geometry of the cylindrical specimens used for tension and cyclic tests and b) specimen with an extensometer mounted on the testing machine.

Two tensile tests were run at a strain rate of 5x10^{-4} s^{-1}. During one of those tests, the sample was repeatedly unloaded/reloaded every other 1.5 % strain. To evaluate the kinematic and isotropic components of the flow stress, the stress σ_{reverse} for which the stress-strain curve upon unloading deviates from linearity by more than 2.5x10^{-4}, was measured. The kinematic stress *X* (also named back stress) corresponds to the center of the elastic domain and the isotropic component, *R* (friction stress, or effective stress) to its half width, so that [27]:

$$X = \frac{\sigma_{\max} + \sigma_{\text{reverse}}}{2} \qquad R = \frac{\sigma_{\max} - \sigma_{\text{reverse}}}{2} \tag{1}$$

where $\sigma_{\max}$ denotes the flow stress reached just before unloading. The same procedure was used for cyclic loading. Since the values of X and R determined that way are sensitive to the portion of the unloading stress-strain curve considered as a reference for linearity, but also to the amount of deviation used to define reverse plastic flow, an alternative method was also used: the automated identification of constitutive equations with isotropic and kinematic hardening by the optimization algorithm available in the Zset finite element code [28] . The results of this second method, described in the appendix, are fully consistent with those obtained by the previous, classical method.

Fully reversed tension-compression tests were run at fixed plastic strain amplitude, $\Delta\varepsilon_p/2$ = 0.15 %, 0.3 %, 0.4 %, 0.5 %, 0.65 %, 0.8 %, 0.95 %, 1.1 % and 1.3 %, with a strain rate of 10^{-3} s^{-1}. In addition, two tension-compression tests were run at fixed stress amplitude, $\Delta\sigma/2$ = 360 or 500 MPa. Most of the tests were interrupted when the stress or strain amplitude varied by less than 1 % within 10 to 20 cycles. A few plastic strain-controlled tests were repeated, and the second test was interrupted at the transition between cyclic hardening and softening, to extract thin foils.

2.3. Deformation-induced microstructure characterization

Thin foils for TEM observations were cut normal to the specimen axis, and after mechanical polishing, electro-polishing was done during 20s at 40V, using a mixture of 90% acetic acid and 10% perchloric acid cooled at 17°C. Conventional TEM (CTEM) observations under bright-field and dark-field imaging were made with a JEOL 2000EX microscope operating at 200 kV. The ambition of the TEM investigation was not a detailed analysis of the link between the grain orientation (or the Schmid factors) and the associated dislocation pattern, but only to give an overall view of the deformation microstructures depending on the loading range and test control mode. To this aim, the microstructures were observed in several grains from several thin foils, for each test condition, and the most typical images reported.

In parallel with this classical approach, the deformation mechanisms during cyclic loading, and in particular twinning/detwinning were monitored at grain-scale by tests run *in situ*, either in a SEM with high-resolution digital image correlation, or under an AFM. The results of these observations have been reported in detail in [29] and will not be repeated here, but referred to in the discussion.

3. Experimental results

3.1. Tensile and cyclic behavior

Figure 2a shows the engineering stress-strain curve of the material, with a 0.2 % yield stress of 300 MPa and an ultimate tensile stress of 900 MPa. Small serrations, indicative of dynamic strain aging, are observed. The evolution of the true stress and its isotropic and kinematic components versus the cumulated plastic strain (which, for monotonic loading, is simply equal to the plastic strain) is plotted on Figure 2b. The isotropic component is initially predominant, but its increase during plastic flow is limited, while the kinematic component rises at the same rate as the flow stress, and becomes quickly, and increasingly predominant (40% of the flow stress at a plastic strain of 0.8%, 70% at 34%).

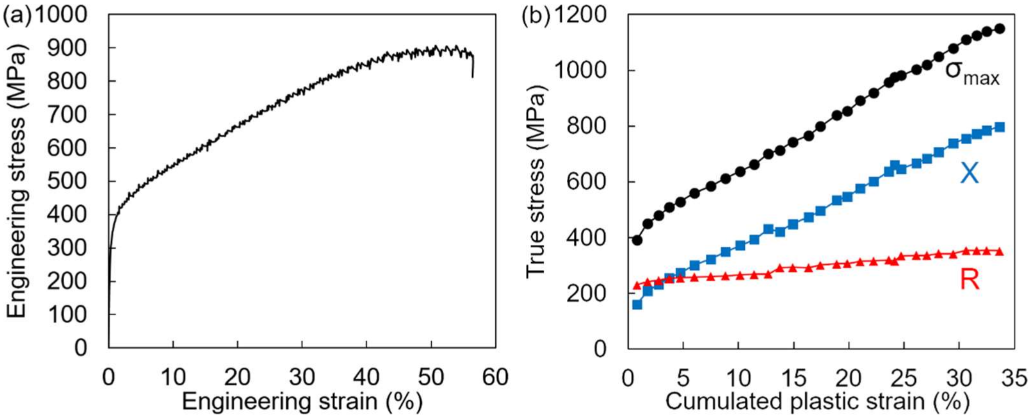

Figure 3: a) Tensile curve along RD at $5x10^{-4}$ s^{-1} and b) associated evolutions of the back stress (X) and friction stress (R)

Figure 3 shows the evolutions of the stress amplitude versus the cumulated plastic strain $4N\Delta\varepsilon_p/2$, (where N denotes the number of cycles) during plastic strain-controlled tests. In all cases, cyclic hardening is first observed, until a cumulated plastic strain which increases with $\Delta\varepsilon_p/2$, as illustrated by Figure 4b. Beyond this amplitude-dependent cumulated plastic strain, a cyclic softening stage, all the more pronounced as the amplitude is large, is observed. The true stress-true strain loops are increasingly elongated and sharp (Fig. 2c). No significant tension-compression asymmetry is observed, contrary to some other studies [19,25].

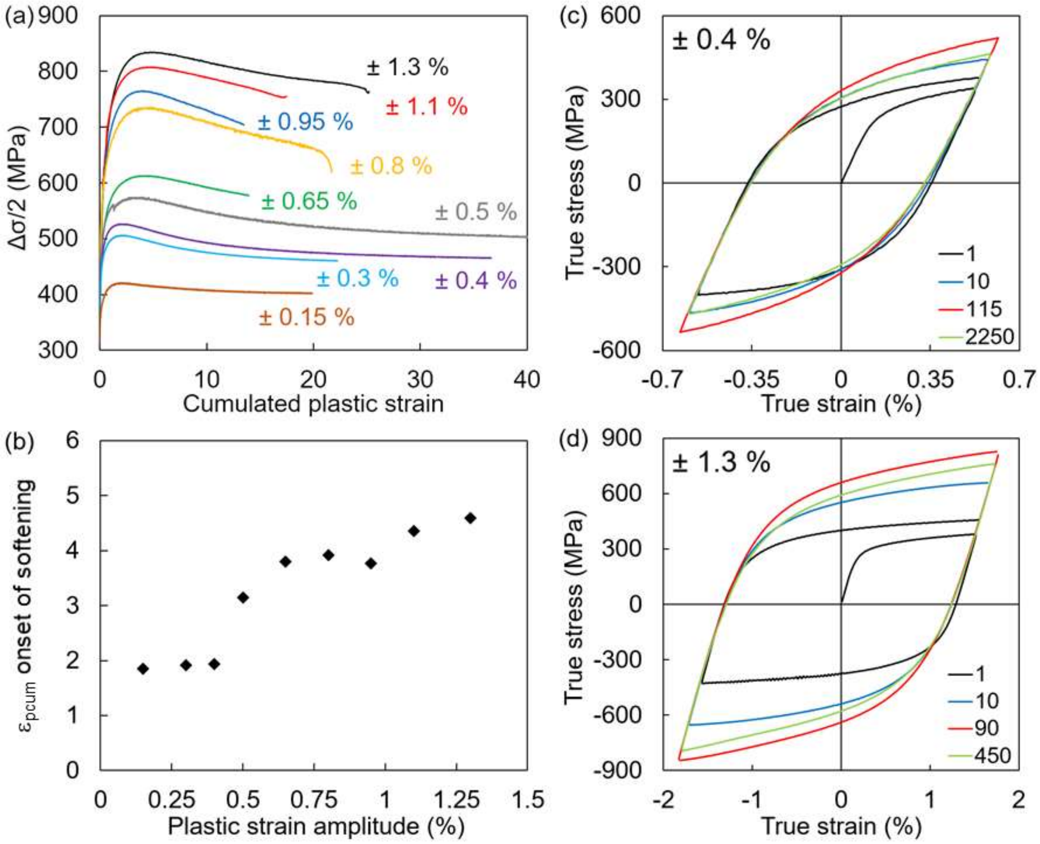

Figure 4: Plastic-strain controlled push-pull tests. a) evolution of the stress amplitude, b) Cumulated plastic strain at the onset of cyclic softening versus $\Delta\varepsilon_p/2$, c) evolution of the stress-strain loops at $\Delta\varepsilon_p/2 = 0.4\%$ and d) $\Delta\varepsilon_p /2= 1.3\%$.

The evolutions of the kinematic and isotropic components of the flow stress with the cumulated plastic strain are plotted on Fig.5a and b, respectively, and compared to those measured under monotonic tension. Under cyclic loading, the increase of the kinematic stress, X, is much slower and less pronounced than under monotonic loading. Figure 5c highlights that cyclic hardening is mostly due to a rise in the kinematic component, but that the isotropic component remains predominant at ± 0.4%. As $\Delta\varepsilon_p/2$ increases, the contributions of X and R to the flow stress become similar, but the kinematic component reaches at most 45 to 50% of the flow stress. While for many metals and alloys, the isotropic stress can reasonably be assumed to depend only on the cumulated plastic strain, as for example, in the popular constitutive model of Lemaitre and Chaboche [30], the dependence of R on the plastic strain amplitude cannot be neglected in the present TWIP steel. In addition, the striking change in shape of the stress-strain loops, and the fact that cyclic hardening is mostly due to a rise of kinematic hardening is not captured by most constitutive models. These two features call for a more complex model, detailed in the appendix.

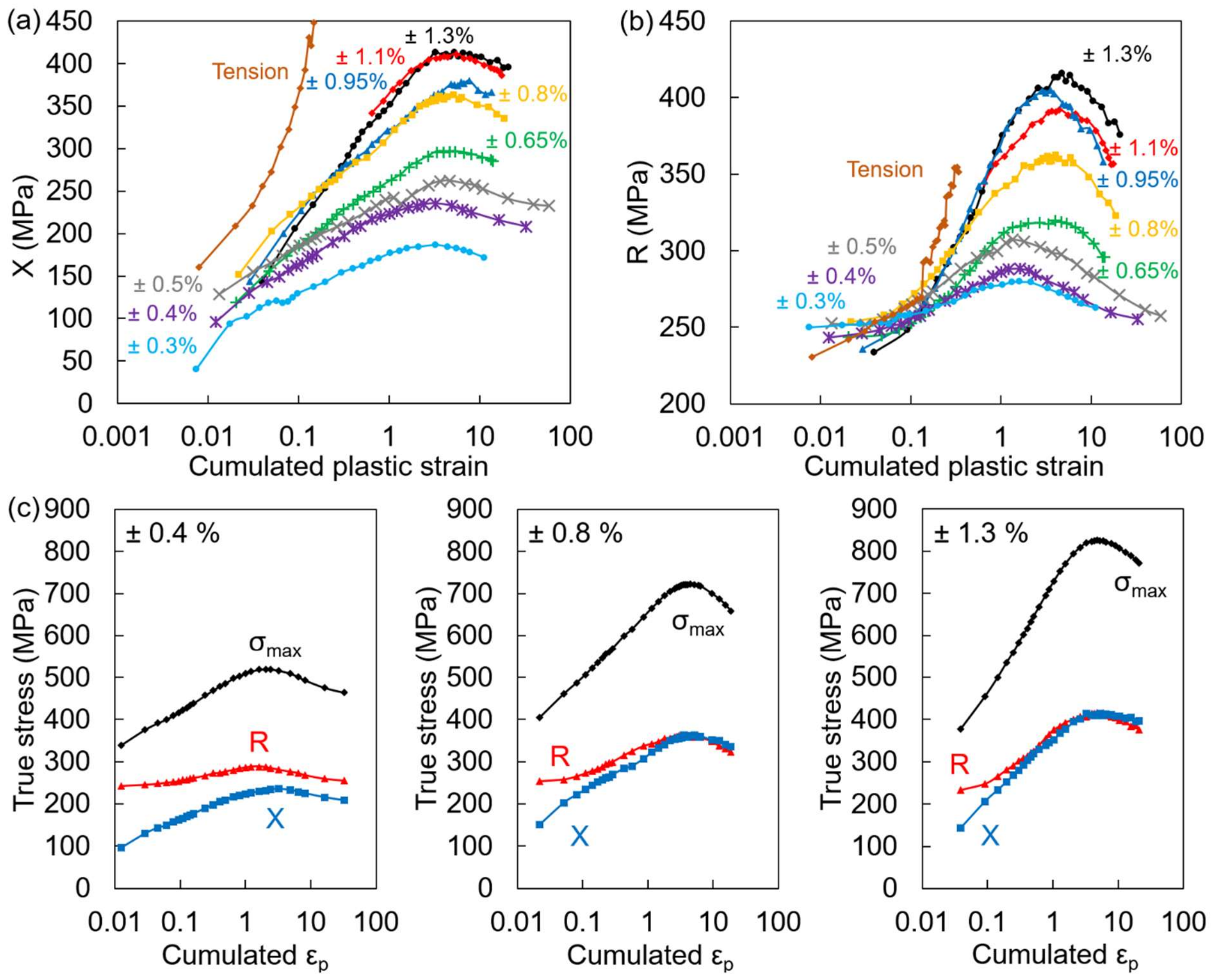

Figure 5: Compared evolutions of a) the back-stress, X, and b) friction stress, R, in tension and plastic strain-controlled push-pull loadings at different amplitudes and c) compared evolutions of X, R and σ_{max} at $\Delta\varepsilon_p/2$ = 0.4%, 0.8% and 1.3%

Figure 6a shows the evolution of the true stress-true strain loops during the tension-compression test run at ± 500 MPa. At the end of the first tensile ramp, a monotonic plastic strain nearly equal to 5 % is reached (0.6 % for the test at ± 360 MPa). Afterwards, the loop shrinks in width, i.e.: the plastic strain amplitude decreases due to cyclic hardening. The evolutions of $\Delta\varepsilon_p/2$ during the two tests run at fixed stress amplitude are plotted on Figure 6b. As for the tests run at fixed plastic strain amplitude, a cyclic softening stage follows the initial cyclic hardening. The evolutions of X and R with the cumulated plastic strain are compared to those measured at $\Delta\varepsilon_p/2$ = 0.3% and 0.5% on Figure 6c and d. While R evolves in a comparable way for both test control modes, X has a relatively high starting value for stress-controlled tests, which is a consequence of the significant monotonic plastic strain during the first loading ramp and of the fast rise of X under monotonic loading (Figure 5a). Then it slightly decreases until a cumulated plastic strain close to 2, and then rises again. This trend is expected, since σ_{max} = X + R (see equation 1) and σ_{max} is kept constant. Thus, if R increases, and then decreases, X = σ_{max} –R should evolve the opposite way.

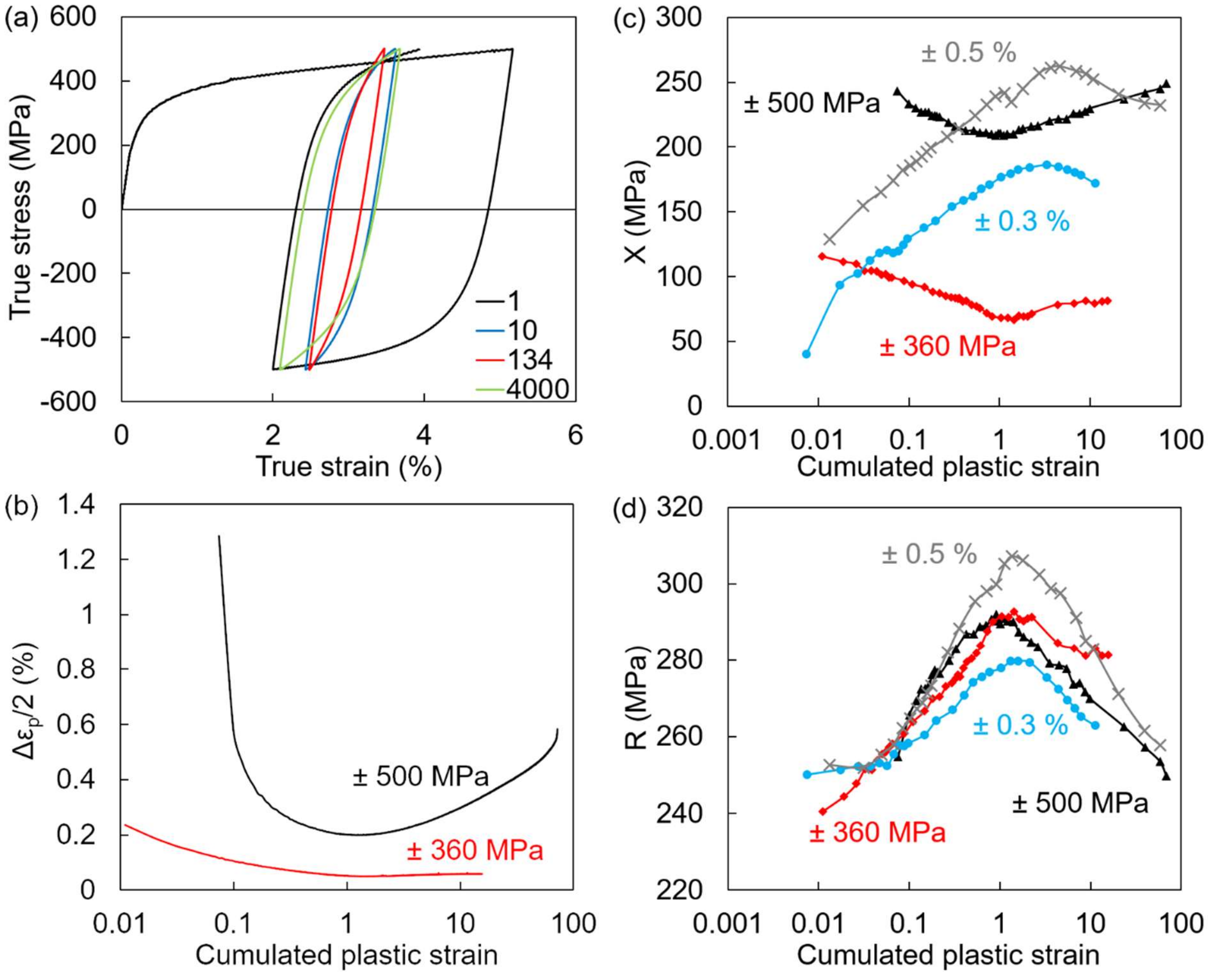

Figure 6: Stress-controlled push-pull tests. a) stress-strain loops at $\Delta\sigma/2$= 500 MPa, b) evolution of the plastic strain amplitude, c) compared evolutions of the back stress, X, and d) compared evolutions of the friction stress, R.

3.2. Fatigue-induced microstructures

CTEM observations performed after the tests run at fixed plastic strain amplitude are presented in Figure 7. At $\Delta\varepsilon_p/2$ = 0.15 %, and 0.3 %, bunches of dislocations, ill-defined dislocation walls, stacking faults (Fig. 7a, b) and scarce twins are observed (Fig. 7e). On fig. 7e, 14 twins are in nearly edge-on position, allowing an estimate of their apparent thickness, which ranges from 6 to 35 nm, while their surface fraction seems to be near 25%. The dislocation density increases with the loading amplitude, and the dislocation and cell walls and appear thinner and well defined (Fig. 7c, d). At $\Delta\varepsilon_p/2$ = 0.8 %, most of the grains exhibit twins along a single plane which tend to form clusters (Fig. 7g). In the grain shown on Fig. 7g, clusters containing up to 13 twins can be observed, and the twin fraction is around 60%. The twin fraction is however quite variable from one grain to the other. In the grains without presence of twins, intense slip bands are superimposed on a background of dislocation cells (Fig. 7c). At $\Delta\varepsilon_p/2$ = 1.3 %, many grains contain twins developed along two or even three different twinning systems (Fig. 7d, h).

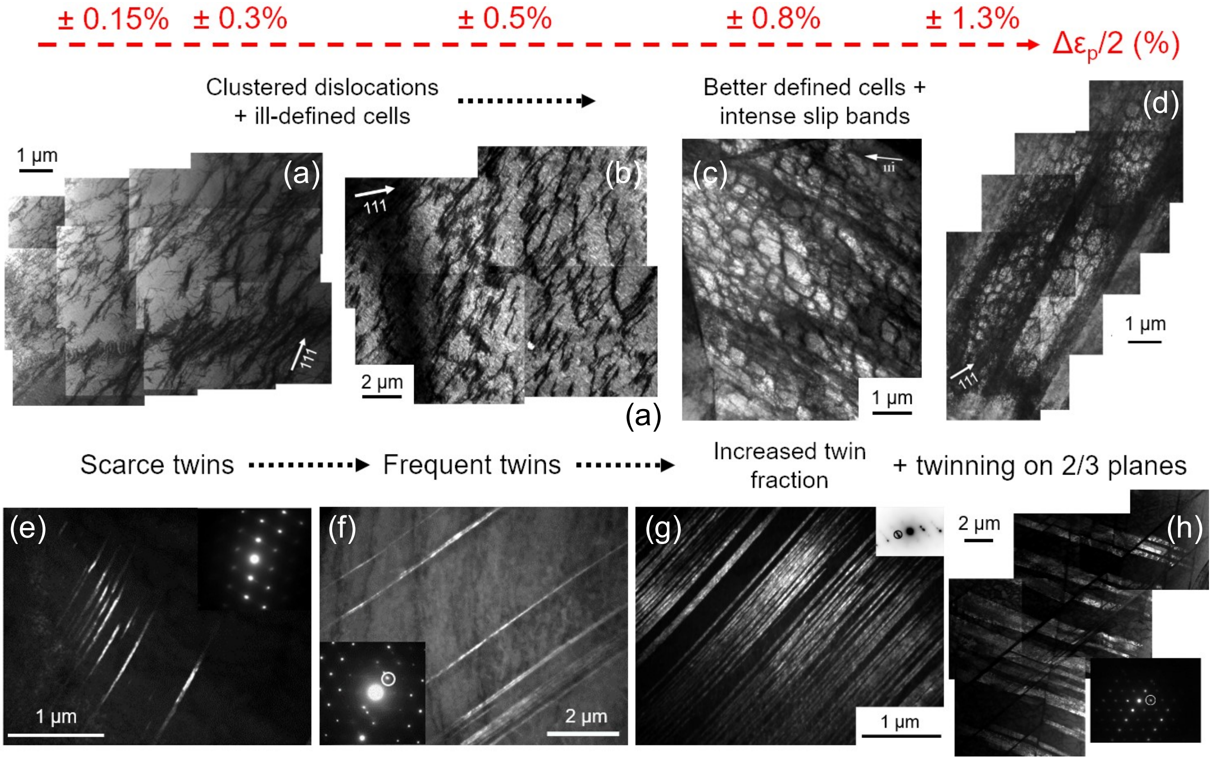

Figure 7: TEM observations, after plastic strain-controlled tests. a)-d) Bright-field micrographs taken in two-beam conditions. Dislocation tangles and poorly defined dislocation walls are observed in a) and b). Defined cells are evidenced in c) and d). Note the presence of an increasing fraction of twins in e)-h). Diffraction patterns are seen in the insert of e)-h). White circles indicate the reflection used for the dark-field micrographs in e)-h).

For $\Delta\varepsilon_p/2$ = 0.5 %, 0.8 %, and 1.3 %, CTEM observations were also made at the end of the cyclic hardening stage, with the aim to discern the underlying microstructural transformations during cyclic softening (Fig 8). For $\Delta\varepsilon_p/2$ = 0.5 %, dislocation walls and channels were predominant in some grains (Fig. 8a), while some grains exhibited dislocation cells (Fig. 8b). For $\Delta\varepsilon_p/2$ = 0.8 % and 1.3 % (Fig. 8c, 8d), dislocation cells were more frequent. The main difference between the end of cyclic hardening (Fig. 8) and a later stage (Fig. 7) was the larger number and better definition of the intense slip bands superimposed on a background of dislocation cells, and the more condensed cell walls, after cyclic softening. The presence, by the end of cyclic hardening, of dislocation cells, usually associated with the last stage of recovery, occurring later in the cyclic softening stage for FCC alloys [31] can seem surprising. However, the transition between hardening and softening was not sudden here, and the stress amplitude remained stationary for about 20 to 25 cycles, before it clearly started to decrease. This might be due to a grain-to-grain heterogeneity in the evolution of the microstructure, with some grains already in the recovery stage and developing cells, while others are still in the hardening stage. If the fraction of the former increases softening becomes visible at the macroscale.

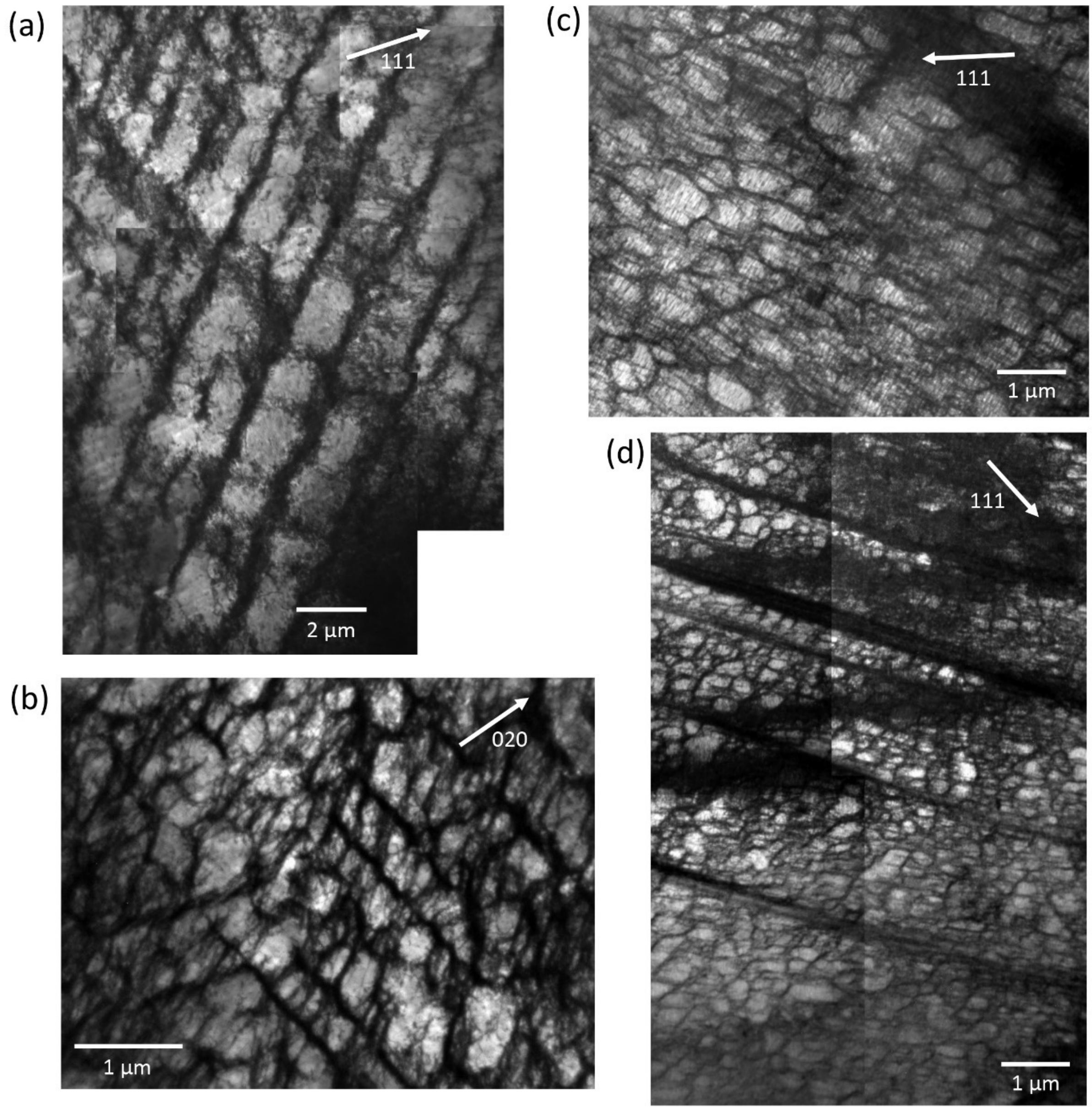

Figure 8. CTEM observations by the end of cyclic hardening for plastic strain-controlled tests. Bright-field micrographs taken in two-beam conditions. a-b) $\Delta\varepsilon_p/2$ = 0.5 %, ε_{pcum} = 3.1, c) $\Delta\varepsilon_p/2$ = 0.8 %, ε_{pcum} = 3.9, d) $\Delta\varepsilon_p/2$ = 1.3 %, ε_{pcum} = 4

CTEM observations performed after the stress-controlled tests are reported in Figure 9. At $\Delta\sigma/2$= 360 MPa, the dislocation density is rather low despite the high cumulated plastic strain (ε_{pcum} = 15.6). The distribution of tangled dislocations is relatively uniform within each grain. Very few, thin and isolated twins are observed. At $\Delta\sigma/2$= 500 MPa (ε_{pcum} = 72), the dislocation density is much higher, especially in series of parallel, dark-looking bands. In-between these bands, regular dislocation distributions are highlighted and suggest ladder-like structures of persistent slip bands. Moreover, the twin density is low, despite the large monotonic plastic strain during the first tensile ramp to 500 MPa. The plastic strain amplitude evolved between $\Delta\varepsilon_p/2$ = 0.3 % and $\Delta\varepsilon_p/2$ = 0.5 % during this test, but the twin density is much lower than after the test run at $\Delta\varepsilon_p/2=0.5\%$, for which the stress amplitude progressively increased from 400 to 570 MPa. The dark field image (Fig. 9f) evidences the presence of some cluster of stacking faults, or remnants of twins after partial detwinning (see the discussion below).

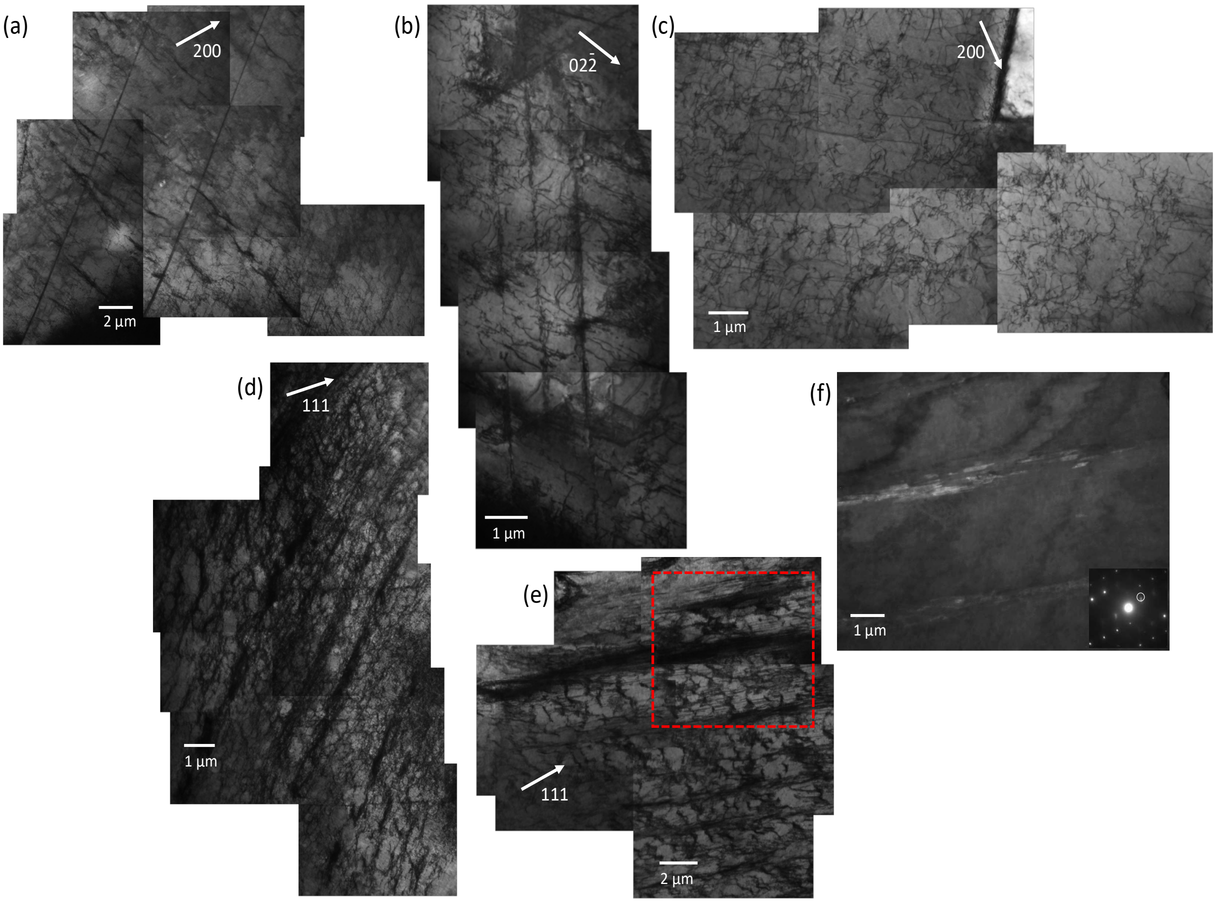

Figure 9: CTEM observations of the microstructures after stress-controlled tests. a)-b)-c): $\Delta\sigma/2$=360 MPa, d)-f): $\Delta\sigma/2$=500 MPa. All the micrographs are taken in bright-field mode and under two-beam conditions except f) which is a dark-field image of the rectangle in e).

4 Discussion

The origin of the rising back stress under cyclic loading has to be discussed in terms of deformation mechanisms, and especially with respect to mechanical twinning. Its lower level as compared to that in monotonic tension (Fig. 5a) also deserves some comments.

As mentioned in the introduction, the evolution of the twinned fraction, during *in situ* push-pull tests run on the present TWIP steel, under fixed stress amplitude or fixed plastic strain amplitude, under an Atomic Force Microscope (AFM) was measured in a few, well oriented grains [29]. Under fixed stress amplitude ($\Delta\sigma/2$= 500 MPa), the twin fraction in all monitored grains was significant after the first ramp, due to nearly 5% monotonic plastic strain, but saturated already from the 2nd cycle, while under fixed plastic strain amplitude ($\Delta\varepsilon_p/2$ = 0.5%), it increased in a ratchetting way during the whole cyclic hardening stage, and stopped increasing at the onset of cyclic softening. It is tempting to correlate these observations to the continuous increase of the back stress until the onset of cyclic softening, under fixed plastic strain amplitude (Fig. 5a), and, under fixed stress amplitude, to the high initial value of the back-stress, and the absence of rise thereof (Fig. 6b). If twinning was, to a large extent, responsible for the kinematic component of the flow stress, its lower value in push-pull than in monotonic tension for the same cumulated plastic strain (Fig. 5a) would also be consistent with the lower twin fraction under cyclic loading. Furthermore, during reversed loading, repeated twinning/detwinning, or alternating twinning on two systems of the same twinning plane, in tension and compression, respectively were observed in most monitored grains [29], rather than multiple twinning along different planes, as observed above 11% monotonic tensile strain in Fe22Mn0.6C [32]. Besides the, strain-induced lattice rotations observed in tension, and which favor further twinning at high strain do not occur in push-pull. This also contributes to a lower twinned fraction at the same cumulated plastic strain. The predominance of the friction stress over the back stress at low plastic strain amplitudes, when twinning is hardly activated, and the relative increase of the latter at high strain amplitudes, when twinning is more active (Fig. 5c) also suggest that mechanical twinning contributes mostly to kinematic hardening. Such trends were also reported for Fe22Mn0.6C and Fe22Mn0.6C3Al, in which the ratio X/σ_{max} was around 43% at $\Delta\varepsilon_p/2$ = 0.5%, 48% at $\Delta\varepsilon_p/2$ = 0.8%, 60% at $\Delta\varepsilon_p/2$ = 1.3% in the former, after 50 push-pull cycles, and 40% at $\Delta\varepsilon_p/2$ = 0.5%, 40% at $\Delta\varepsilon_p/2$ = 0.8%, and 51% at $\Delta\varepsilon_p/2$ = 1.3%, in the latter. Besides, the internal stress contributed more to the flow stress in Fe22Mn0.6C, which exhibited more profuse twinning, than in Fe22Mn0.6C3Al. It is worth noting that the already high back stress in Fe22Mn0.6C3Al despite its more limited twinning activity implies that twinning is not the only source of back stress in these steels. This was also underlined by Zhi et al. [33], and will be discussed below.

The sources of back stress in a polycrystal can be of transgranular or intergranular nature. In the present study, TEM observations did not reveal dislocation pileups against twin boundaries. Besides, by measuring the distribution of Geometrically Necessary Dislocations (GND) density in Fe22Mn0.6C(3Al), after interrupted tensile tests, Zhi et al. [33] also reported much less GND pileups against deformation twins than against grain boundaries. This might partly be due compatibility stresses near the twin/matrix interface resulting from the elastic anisotropy of their lattices, favoring the activation of coplanar rather than intersecting slip systems, as shown by Richeton et al. [34]. In addition, after the cyclic tests, dislocation cells often coexisted with twins in the same grain, and the dislocation cell size was generally smaller than the distance between the twins. Thus, cell walls -rather than twin boundaries- probably control the dislocations mean free path, and most dislocations do not encounter any twin boundary. The dynamic Hall-Petch effect attributed to twin boundaries is thus probably even less effective under cyclic loading than in tension, and the contribution of twins to the intragranular component of the back stress is probably limited. The latter might mostly be due to the long-range internal stresses associated with the heterogeneous, “composite” microstructure made of “hard”, dislocations-rich and “soft”, dislocations-poor areas.

However, twinned grains were shown numerically by Arul Kumar et al. [35–37] to undergo a substantial back stress from neighboring grains, especially those poorly oriented to accommodate – through local plastic flow - the stress concentration at grain boundaries impinged by the twins. Compared to the HCP metals, for which these computations were made, the smaller degree of plastic anisotropy of FCC TWIP steel grains should make the accommodation of the twin-induced stress concentrations on the grain boundaries somewhat easier. On the other hand, the back-stress induced on a twinned grain by unfavorably oriented neighboring grains, which is proportional to the shear modulus (see equation 16 in [38]) would be substantially higher. In other words, in TWIP steels as well as in HCP metals, twinning might contribute to a back stress of intergranular origin. This deviates from the “dynamic Hall-Petch” model, which rather lays emphasis on the barriers that twin boundaries would constitute for impinging dislocations, inside the grain. The intergranular back stress would be expected to rise with the fraction of twinned grains, and thus much faster in tension than under reversed cyclic loading, at fixed plastic strain amplitude, and not to rise at all at fixed stress amplitude, in accordance to the present observations. Such an effect has indeed been integrated semi-empirically in a mean-field crystal plasticity model for such steels, by McCormack et al. [39].

The physical mechanisms of cyclic softening also raise questions, even though it is much more modest than the initial hardening stage. In the present study, cyclic softening was associated mostly with a decrease of the isotropic component of the flow stress, , and the development of intense deformation bands. As indicated in the introduction, the softening stage in various TWIP steels has been attributed to a disordering of C-Mn SRO, and the consecutive the development of strain localization bands [5], or to a progressive reduction in dislocation density [16,17]. While the latter two explanations can be directly supported by TEM observations, a direct proof of the first one -and not just of its consequences: a less planar glide and the appearance of strain localization bands - is more difficult to obtain. Small Angle neutron scattering analysis of C-Mn clusters, as those performed by Kang et al. [39] or Song et al [40] after tensile tests on TWIP steel, might also be performed before cyclic loading as well as at various plastic strain amplitudes and cumulated plastic strains, to document any modification of the SRO, and to compare the effect of monotonic and reversed cyclic loading on the C-Mn clusters. Concerning the latter point, Pettinari-Sturmel et al. [41] have shown through *in situ* tests in a TEM, that dislocation-induced shearing and perturbation of SRO can be reversible when the dislocations glide back along the same plane, due to unloading. The dislocation-induced reduction of the degree of SRO might thus be less effective under reversed cyclic loading than under monotonic loading at the same cumulated plastic strain. Furthermore, a sufficient stress must be achieved on the leading dislocation to allow it to shear an ordered zone [41]. This might be the reason why cyclic softening in the present TWIP steel (and many others) is not observed at low plastic strain amplitude (the curve for $\Delta\varepsilon_p/2$ = 0.15% on Fig. 3a rather shows a steady-state, directly after cyclic hardening). It is also interesting to note that the cumulated plastic strain at the onset of macro-scale cyclic softening is not constant, but rises with $\Delta\varepsilon_p$, as illustrated by Fig. 4b. This is rather unexpected, since the higher $\Delta\varepsilon_p$, the faster and stronger is cyclic hardening (Fig. 4a), and thus the sooner a hypothetic microscale critical stress would be reached. These observations suggest that neither the peak stress, nor the cumulated plastic strain -which more or less reflects the cumulated dislocation flux- fully control the alteration of SRO, but that qualitative parameters - like the activation of a single or several slip systems in a grain -also play a role in the disordering kinetics. Multiple slip, favored by high loading amplitudes, might actually less effectively alter the SRO than single slip. There is clearly room for in-depth research on SRO evolution under cyclic loading.

Conclusions

* Push-pull tests run at fixed plastic strain amplitude or fixed stress amplitude on a TWIP steel both lead to a succession of cyclic hardening, and cyclic softening whose importance rose with the loading amplitude.

* At fixed plastic strain amplitude, cyclic hardening was mostly due to a rise in the internal stress, attributed to the development of heterogeneous dislocation distributions, and to the increasing twin fraction. The rise of the internal stress with the cumulated plastic strain was however much slower than in tension, and this stress constituted at most 50% of the flow stress, at high stress amplitude, while it reached 70% in tension.

*At fixed stress amplitude, cyclic hardening was mostly due to a rise of the friction stress, while the internal stress, relatively high after the first loading ramp -which induced significant monotonic plastic flow and mechanical twinning- first decreased during cyclic loading.

* In both cases, the subsequent cyclic softening started all the later in terms of cumulated plastic strain as the loading amplitude was high. Softening was associated mainly with a decrease of the friction stress, and the development of intense deformation bands. It might be the consequence of a dislocation-induced disordering of SRO, but this deserves further investigation.

* Although mechanical twinning/detwinning accommodates part of the cyclic plasticity in this TWIP steel, the kinematic hardening that it provides is not of intragranular nature, but rather intergranular.

* Constitutive equations with a special form of non-linear kinematic hardening and a strain amplitude-dependent isotropic hardening captured well the cyclic behavior and the evolution of stress-strain loops shapes, at fixed plastic strain amplitude.

Acknowledgments

The authors are grateful for the support of Arcelor Mittal who provided the material and samples studied in this work, and more specifically to Bastien Weber and Nicolas Charbonnier for their continued interest in this work.

Conflict of interest.

The authors declare that they have no conflict of interest.

References

[1] O. Bouaziz, S. Allain, C.P. Scott, P. Cugy, D. Barbier, High manganese austenitic twinning induced plasticity steels: A review of the microstructure properties relationships, Current Opinion in Solid State & Materials Science. 15 (2011) 141–168. https://doi.org/10.1016/j.cossms.2011.04.002.

[2] B.C. De Cooman, Y. Estrin, S.K. Kim, Twinning-induced plasticity (TWIP) steels, Acta Materialia. 142 (2018) 283–362. https://doi.org/10.1016/j.actamat.2017.06.046.

[3] P. Guo, L. Qian, J. Meng, F. Zhang, L. Li, Low-cycle fatigue behavior of a high manganese austenitic twin-induced plasticity steel, Materials Science and Engineering A-Structural Materials Properties Microstructure and Processing. 584 (2013) 133–142. https://doi.org/10.1016/j.msea.2013.07.020.

[4] C.W. Shao, P. Zhang, R. Liu, Z.J. Zhang, J.C. Pang, Z.F. Zhang, Low-cycle and extremely-low-cycle fatigue behaviors of high-Mn austenitic TRIP/TWIP alloys: Property evaluation, damage mechanisms and life prediction, Acta Materialia. 103 (2016) 781–795. https://doi.org/10.1016/j.actamat.2015.11.015.

[5] C.W. Shao, P. Zhang, R. Liu, Z.J. Zhang, J.C. Pang, Q.Q. Duan, Z.F. Zhang, A remarkable improvement of low-cycle fatigue resistance of high-Mn austenitic TWIP alloys with similar tensile properties: Importance of slip mode, Acta Materialia. 118 (2016) 196–212. https://doi.org/10.1016/j.actamat.2016.07.034.

[6] C.W. Shao, P. Zhang, Y.K. Zhu, Z.J. Zhang, J.C. Pang, Z.F. Zhang, Improvement of low-cycle fatigue resistance in TWIP steel by regulating the grain size and distribution, Acta Materialia. 134 (2017) 128–142. https://doi.org/10.1016/j.actamat.2017.05.004.

[7] C.W. Shao, P. Zhang, Z.J. Zhang, R. Liu, Z.F. Zhang, Forecasting Low-Cycle Fatigue Performance of Twinning-Induced Plasticity Steels: Difficulty and Attempt, Metallurgical and Materials Transactions A-Physical Metallurgy and Materials Science. 48A (2017) 5833–5848. https://doi.org/10.1007/s11661-017-4360-y.

[8] C.W. Shao, P. Zhang, Z.J. Zhang, Z.F. Zhang, Butterfly effect in low-cycle fatigue:

Importance of microscopic damage mechanism, Scripta Materialia. 140 (2017) 76–81. https://doi.org/10.1016/j.scriptamat.2017.07.007.

[9] J.A. Benito, R. Cobo, W. Lei, J. Calvo, J.M. Cabrera, Stress-strain response and microstructural evolution of a FeMnCAl TWIP steel during tension-compression tests, Materials Science and Engineering A-Structural Materials Properties Microstructure and Processing. 655 (2016) 310–320. https://doi.org/10.1016/j.msea.2016.01.004.

[10] H.K. Yang, V. Doquet, Z.F. Zhang, Fatigue crack growth in two TWIP steels with different stacking fault energies, International Journal of Fatigue. 98 (2017) 247–258. https://doi.org/10.1016/j.ijfatigue.2017.01.034.

[11] Y. Chen, Y.J. Luo, Y.F. Shen, Y. Liu, R.D.K. Misra, Cumulative contribution of grain structure and twin boundaries on cyclic deformation behavior of a 20Mn-0.6C-TWIP steel: Experimental and theoretical analysis, Materials Science and Engineering A-Structural Materials Properties Microstructure and Processing. 767 (2019). https://doi.org/10.1016/j.msea.2019.138415.

[12] Y. Wu, D. Tang, H. Jiang, Z. Mi, Y. Xue, H. Wu, Low Cycle Fatigue Behavior and Deformation Mechanism of TWIP Steel, Journal of Iron and Steel Research International. 21 (2014) 352–358. https://doi.org/10.1016/S1006-706X(14)60054-6.

[13] A.S. Hamada, A. Jarvenpaa, M. Honkanen, M. Jaskari, D.A. Porter, L.P. Karjalainen, Effects of cyclic pre-straining on mechanical properties of an austenitic microalloyed high-Mn twinning-induced plasticity steel, in: M. Guagliano, L. Vergani (Eds.), 2014: pp. 47–52. https://doi.org/10.1016/j.proeng.2014.06.222.

[14] S.W. Song, J.-N. Kim, H.J. Seo, T. Lee, C.S. Lee, Effects of carbon content on the tensile and fatigue properties in hydrogencharged Fe-17Mn-xC steels: The opposing trends, Materials Science and Engineering A-Structural Materials Properties Microstructure and Processing. 724 (2018) 469–476. https://doi.org/10.1016/j.msea.2018.03.117.

[15] C.J. Ruesing, T. Niendorf, A. Frehn, H.J. Maier, Low-cycle fatigue behavior of TWIP steel - Effect of grain size, in: G. Clark, C. Wang (Eds.), 2014: pp. 1603-+. https://doi.org/10.4028/www.scientific.net/AMR.891-892.1603.

[16] T. Niendorf, C. Lotze, D. Canadinc, A. Frehn, H.J. Maier, The role of monotonic pre-deformation on the fatigue performance of a high-manganese austenitic TWIP steel, Materials Science and Engineering A-Structural Materials Properties Microstructure and Processing. 499 (2009) 518–524. https://doi.org/10.1016/j.msea.2008.09.033.

[17] H.-G. Lambers, C.J. Ruesing, T. Niendorf, D. Geissler, J. Freudenberger, H.J. Maier, On the low-cycle fatigue response of pre-strained austenitic Fe61Mn24Ni6.5Cr8.5 alloy showing TWIP effect, International Journal of Fatigue. 40 (2012) 51–60. https://doi.org/10.1016/j.ijfatigue.2012.01.002.

[18] A.S. Hamada, L.P. Karjalainen, J. Puustinen, Fatigue behavior of high-Mn TWIP steels, Materials Science and Engineering A-Structural Materials Properties Microstructure and

Processing. 517 (2009) 68–77. https://doi.org/10.1016/j.msea.2009.03.039.

[19] X. Wang, Z.Y. Liang, R.D. Liu, M.X. Huang, Evolution of dislocations and twins in high cycle fatigue of a twinning-induced plasticity steel, Materials Science and Engineering A-Structural Materials Properties Microstructure and Processing. 647 (2015) 249–255. https://doi.org/10.1016/j.msea.2015.09.017.

[20] P. Ma, J. Shen, S. Liu, Q. Zhou, L. Zhao, L. Qian, Effects of Strain Rate on Low-Cycle Fatigue Behaviors of Fe-22Mn-0.6C TWIP Steel, Advanced Engineering Materials. 21 (2019). https://doi.org/10.1002/adem.201801042.

[21] A.S. Hamada, L.P. Karjalainen, A. Ferraiuolo, J. Gil Sevillano, F. de las Cuevas, G. Pratolongo, M. Reis, Fatigue Behavior of Four High-Mn Twinning Induced Plasticity Effect Steels, Metallurgical and Materials Transactions A-Physical Metallurgy and Materials Science. 41A (2010) 1102–1108. https://doi.org/10.1007/s11661-010-0193-7.

[22] Y.W. Kim, G. Kim, S.-G. Hong, C.S. Lee, Energy-based approach to predict the fatigue life behavior of pre-strained Fe-18Mn TWIP steel, Materials Science and Engineering A-Structural Materials Properties Microstructure and Processing. 528 (2011) 4696–4702. https://doi.org/10.1016/j.msea.2011.02.068.

[23] L.P. Karjalainen, A. Hamada, R.D.K. Misra, D.A. Porter, Some aspects of the cyclic behavior of twinning-induced plasticity steels, Scripta Materialia. 66 (2012) 1034–1039. https://doi.org/10.1016/j.scriptamat.2011.12.008.

[24] G. Chalant and L. Rémy, The Influence of Slip Character on the Low Cycle Fatigue Behaviour. Proc. 5th Int. Conf. Strength Metals and Alloys, Aachen, Germany, August 27–31, 1979, Vol. 2, (1979) 1195-1200

[25] A.A. Saleh, E.V. Pereloma, B. Clausen, D.W. Brown, C.N. Tome, A.A. Gazder, On the evolution and modelling of lattice strains during the cyclic loading of TWIP steel, Acta Materialia. 61 (2013) 5247–5262. https://doi.org/10.1016/j.actamat.2013.05.017.

[26] S. Allain, J.-P. Chateau, O. Bouaziz, S. Migot, N. Guelton, Correlations between the calculated stacking fault energy and the plasticity mechanisms in Fe–Mn–C alloys, Materials Science and Engineering: A. 387–389 (2004) 158–162. https://doi.org/10.1016/j.msea.2004.01.059.

[27] J.I. Dickson, J. Boutin, L. Handfield, A comparison of 2 simple methods for measuring cyclic internal and effective stresses, Materials Science and Engineering. 64 (1984) L7–L11. https://doi.org/10.1016/0025-5416(84)90083-1.

[28] Z-set. Non-linear materials & structures analysis suite: http://www.zset-software.com/

[29] C. D'Hondt, V. Doquet, J.P. Couzinie, Direct monitoring of twinning/detwinning in a TWIP steel under reversed cyclic loading, Materials Science and Engineering A-Structural Materials Properties Microstructure and Processing. 814 (2021). https://doi.org/10.1016/j.msea.2021.141250.

[30] J. Lemaitre, J.L. Chaboche, A. Benalla, R. Desmorat, Mécanique des matériaux solides. 3ème version, Dunod, Paris, 2020.

[31] M.S. Pham, C. Solenthaler, K.G.F. Janssens, S.R. Holdsworth, Dislocation structure evolution and its effects on cyclic deformation response of AISI 316L stainless steel, Mater. Sci. Engng. A 528 (2011) 3261–3269, https://doi:10.1016/j.msea.2011.01.015

[32] H.K. Yang, V. Doquet, Z.F. Zhang, Micro-scale measurements of plastic strain field, and local contributions of slip and twinning in TWIP steels during in situ tensile tests, Materials Science and Engineering A-Structural Materials Properties Microstructure and Processing. 672 (2016) 7–14. https://doi.org/10.1016/j.msea.2016.06.064.

[33] H. Zhi, S. Antonov, C. Zhang, Z. Guo, Y. Su, Origins of back stress strengthening in Fe-22Mn-0.6C (-3Al) TWIP steels, Materials Science and Engineering A-Structural Materials Properties Microstructure and Processing. 792 (2020). https://doi.org/10.1016/j.msea.2020.139834.

[34] T. Richeton, I. Tiba, S. Berbenni, O. Bouaziz, Analytical expressions of incompatibility stresses at 3 111 twin boundaries and consequences on single-slip promotion parallel to twin plane, Philosophical Magazine. 95 (2015) 12–31. https://doi.org/10.1080/14786435.2014.984787.

[35] M.A. Kumar, A.K. Kanjarla, S.R. Niezgoda, R.A. Lebensohn, C.N. Tome, Numerical study of the stress state of a deformation twin in magnesium, Acta Materialia. 84 (2015) 349–358. https://doi.org/10.1016/j.actamat.2014.10.048.

[36] M.A. Kumar, I.J. Beyerlein, C.N. Tome, Effect of local stress fields on twin characteristics in HCP metals, Acta Materialia. 116 (2016) 143–154. https://doi.org/10.1016/j.actamat.2016.06.042.

[37] M. Arul Kumar, I.J. Beyerlein, R.A. Lebensohn, C.N. Tomé, Role of alloying elements on twin growth and twin transmission in magnesium alloys, Materials Science and Engineering: A. 706 (2017) 295–303. https://doi.org/10.1016/j.msea.2017.08.084.

[38] S.J. McCormack, W. Wen, E.V. Pereloma, C.N. Tome, A.A. Gazder, A.A. Saleh, On the first direct observation of de-twinning in a twinning-induced plasticity steel, Acta Materialia. 156 (2018) 172–182. https://doi.org/10.1016/j.actamat.2018.06.029.

[39] M. Kang, E. Shin, W. Woo, Y.-K. Lee, Small-angle neutron scattering analysis of Mn-C clusters in high-manganese 18Mn-0.6C steel, Materials Characterization. 96 (2014) 40–45. https://doi.org/10.1016/j.matchar.2014.07.010.

[40] W. Song, J.E. Houston, Local Deformation and Mn-C Short-Range Ordering in a High-Mn Fe-18Mn-0.6C Steel, Metals. 8 (2018). https://doi.org/10.3390/met8050292.

[41] F. Pettinari-Sturmel, J. Douin, A. Coujou, N. Clement, Characterisation of short-range order using dislocations, Zeitschrift Fur Metallkunde. 97 (2006) 200–204. https://doi.org/10.3139/146.101243.

[42] J.L. Chaboche, K. Dang Van, G. Cordier, Modelization of the Strain Memory Effect on the Cyclic Hardening of 316 Stainless Steel, in: International Association For Structural Mechanics in Reactor Technology - IASMIRT 5, Jaeger T.A., Boley B.A., Berlin, 1979: pp. 1–10. http://www.lib.ncsu.edu/resolver/1840.20/26854.

Appendix: Constitutive equations

In this appendix, the formulation of a constitutive model and its identification from the true stress-true strain loops recorded during the push-pull tests run at fixed plastic strain amplitude are described.

Considering the quasi absence of texture of the steel, Von Mises isotropic flow criterion are used. Three kinematic hardening variables, X_1, X_2 and X_3, as well as an isotropic variable R are included, so that the flow criterion reads:

$$J_2(\sigma - X_1 - X_2 - X_3) - R = 0 \tag{A1}$$

To capture the change in shape of the stress-strain loops, a modified version of the classical non-linear kinematic hardening model is used, like in the previous work of Yang et al. [32] :

$$dX_i = \frac{2}{3} C_i d\epsilon_p - \varphi_i(p) D_i X_i dp \quad , \text{i = 1, 2, 3} \tag{A2}$$

where C_1, C_2, C_3, D_1, D_2, D_3 are materials parameters, and p denotes the cumulated plastic strain:

$$\delta p = \sqrt{\frac{2}{3} \delta\varepsilon_p : \delta\varepsilon_p} \tag{A3}$$

$\varphi_i(p)$ are three functions of p:

$$\varphi_i(p) = \varphi_{mi} + (1 - \varphi_{mi}) e^{-\omega_i p} \quad , \text{i = 1, 2, 3} \tag{A4}$$

where φ_{m1} , φ_{m2}, φ_{m3}, ω_1 , ω_2 , ω_3 are materials parameters. $\varphi_{mi} < 1$ reflects cyclic hardening and more and more elongated stress-strain loops.

In the initial model from Lemaitre and Chaboche [30], cyclic isotropic hardening and softening are just described by:

$$R = R_0 + Q_1(1 - e^{-b_1 p}) + Q_2(1 - e^{-b_2 p}) \tag{A5}$$

where R_0, Q_1, Q_2, b_1, b_2 are materials constants. $Q_1 > 0$ reflects cyclic hardening, and $Q_2 < 0$ cyclic softening. To capture the amplitude-dependent evolution of the isotropic variable, a model initially proposed by Chaboche et al. to capture prestrain memory effects [42] is used instead, in which Q_1, Q_2 are considered as functions of :

$$Q_i = Q_{sati} - (Q_{sati} - Q_{0i})e^{-2\Delta\epsilon_p\mu_i}, i = 1,2 \tag{A6}$$

where R_0, Q_{01}, Q_{02}, Q_{sat1}, Q_{sat2}, μ_1, μ_2 are materials parameters.

The optimization module of the Zset finite element code was used to obtain the 21 materials parameters that allow a good description of the recorded stress-strain loops. These coefficients are gathered in table A1. Measured and computed stress-strain loops and stress amplitude evolutions are compared on Figure A1a-f. The evolution of the loop shape is well captured, as well as the transition from cyclic hardening to softening. The evolutions of the kinematic and isotropic components measured with the method based on a deviation from linearity upon unloading are retrieved, which confirms their relevance.

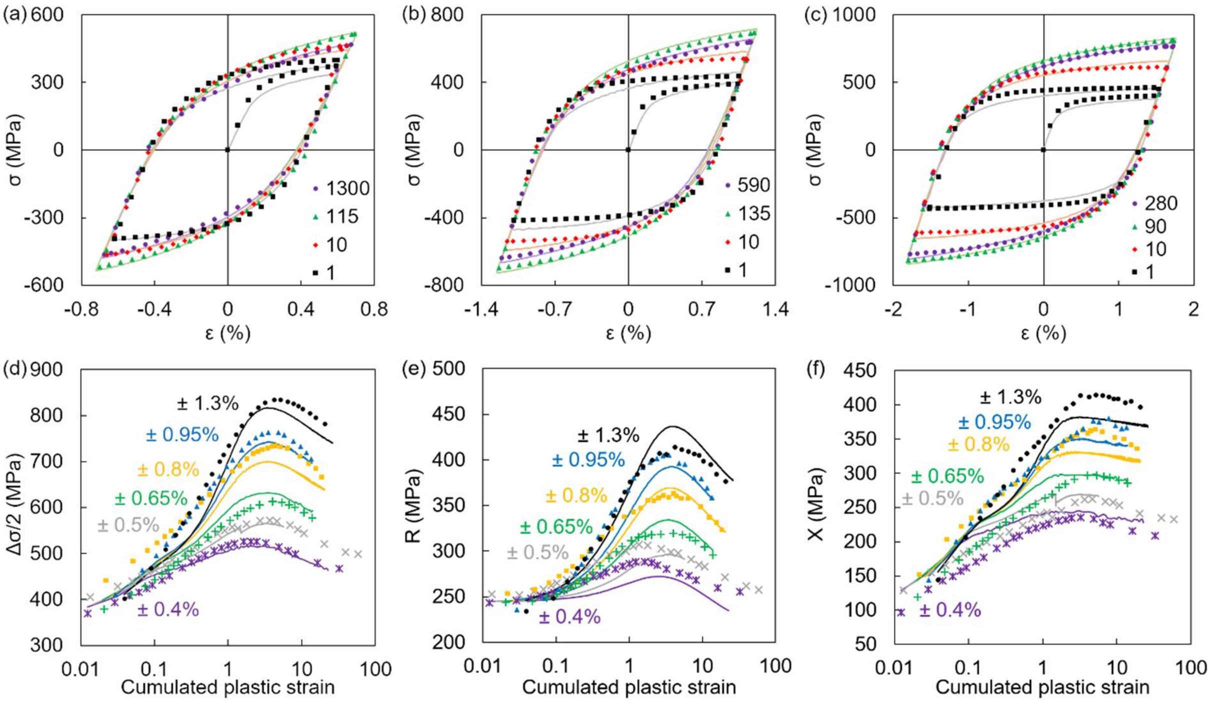

Figure A1. Comparison of measured and simulated behavior.

Hardening				
R_1	Q_{01} (MPa)	Q_{sat1} (MPa)	μ_1	b_1
	-146	320	59	0.88
X_1	C_1 (MPa)	D_1	ϕ_{m1}	ω_1
	41707	1941	0.23	42
X_2	C_2 (MPa)	D_2	ϕ_{m2}	ω_2
	29102	350	0.29	2
Softening				
R_2	Q_{02} (MPa)	Q_{sat2} (MPa)	μ_2	b_2
	56	-114	139	0.08
X_3	C_3 (MPa)	D_3	ϕ_{m3}	ω_3
	51550	1232	2.3	0.05

TABLE AI. Parameters of the constitutive equations